Kroon, D., Zachos, J.C., and Richter, C. (Eds.)
Proceedings of the Ocean Drilling Program, Scientific Results Volume 208

4. Data Report: Revised Magnetostratigraphy and Magnetic Mineralogy of Sediments from Walvis Ridge, Leg 208[1]

Julie Bowles[2]

ABSTRACT

We report the paleomagnetic and rock magnetic results from discrete sample analysis of sediments from Walvis Ridge, Leg 208 of the Ocean Drilling Program. In an effort to refine the shipboard magnetostratigraphy, alternating field and thermal demagnetization of discrete samples were carried out, predominantly on samples from Sites 1262 and 1267. Results are generally consistent with the shipboard pass-through cryomagnetometer data, though in some cases the discrete samples resolved ambiguities in the reversal record. Significantly, the C24r/C24n reversal boundary was identified at Sites 1262 and 1267, and most boundaries in the Paleocene and Upper Cretaceous sections are now identified to within 10–30 cm. Magnetic mineralogy results show that prior to the late Miocene, the predominant detrital magnetic component was coarse-grained magnetite and that after the late Miocene, titanomagnetite has also been present. This suggests a possible change in detrital source at that time.

INTRODUCTION

Shipboard magnetostratigraphic results from pass-through cryomagnetometer measurements on half-cores provided disappointing results for many Ocean Drilling Program (ODP) Leg 208 sites. The easily deformed, carbonate-rich sediments produced a frequently noisy inclina-

[1]Bowles, J., 2006. Data report: revised magnetostratigraphy and magnetic mineralogy of sediments from Walvis Ridge, Leg 208. *In* Kroon, D., Zachos, J.C., and Richter, C. (Eds.), *Proc. ODP, Sci. Results,* 208: College Station, TX (Ocean Drilling Program), 1–24. doi:10.2973/odp.proc.sr.208.206.2006
[2]Scripps Institute of Oceanography, University of California San Diego, 9500 Gilman Drive, MC 0220, La Jolla CA 92093, USA. Present address: Department of Geology and Geophysics, University of Hawaii, 1680 East-West Road, Honolulu HI 96822, USA.
bowlesj@hawaii.edu

Initial receipt: 6 October 2005
Acceptance: 22 June 2006
Web publication: 30 October 2006
Ms 208SR-206

tion signal and an overprint or deformation that resulted in a pervasive declination bias (Zachos, Kroon, Blum, et al., 2004; Bowles, submitted [N1]). The magnetostratigraphy was difficult or impossible to interpret at most sites in sediments above the Paleocene/Eocene (P/E) boundary. Below this boundary, increases in magnetic susceptibility and remanent intensity appear to be accompanied by an increase in the signal-to-noise ratio, and most reversal boundaries were identified.

The present study reports results from postcruise analyses of discrete samples. These samples, from the less-disturbed center of core and measured in a low-noise environment, were taken with the hope of improving the magnetostratigraphic record. In addition to an overall refinement of this record, one of the major goals was the identification of the C24r/C24n reversal just above the P/E boundary. This critical boundary would play an important role in determining the timing and completeness of the sedimentary record following the Paleocene/Eocene Thermal Maximum (PETM). We were unable to accurately place this boundary based solely on the shipboard measurements.

Results from the discrete samples unfortunately did little to refine most of the magnetostratigraphy. However, targeted dense sampling over the C24r/C24n interval allowed us to identify this boundary at the two deepest sites, Sites 1262 (27°11.15′S, 1°34.62′E; 4755 m water depth) and 1267 (28°5.88′S, 1°42.66′E; 4355 m water depth) (Fig. F1). Minor revisions and refinements to the Paleocene and Cretaceous reversal record were also achieved. We further report results from rock magnetic experiments.

The present-day inclination at the study site is –65°, whereas the geocentric axial dipole (GAD) value for the site latitude is 48°. However, the paleolatitude of the site is probably ~5°–7° further south during the Paleocene (O'Connor and Duncan, 1990), corresponding to steeper GAD inclinations of 53°–56°.

F1. Leg 208 sites, p. 9.

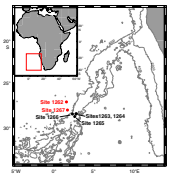

SAMPLING AND METHODS

Discrete samples were taken from the working half of the cores in standard 8-cm^3 cubes. A few samples were taken with small glass tubes, 3 cm long by 1 cm in diameter and etched with a fiducial line. These samples are indicated by a "t" in front of the sample name in Table AT1 of the "Appendix," p. 8. Coarse sampling (one sample per core section) of Hole A from each site was accomplished shipboard, while sampling of critical intervals at denser spacing (as much as 10 cm) was carried out postcruise. These critical intervals included the upper Paleocene to lower Eocene interval containing the C24r/C24n boundary at Sites 1262, 1266, and 1267. We also densely sampled several other reversal boundaries, predominantly in the Paleocene and Cretaceous, in the hope of clarifying or refining the reversal position. It should be noted that many of the cores sampled postcruise were characterized by numerous small cracks on the split surface. These were not desiccation cracks, as the cores were still quite moist, and we were unable to determine the origin of these cracks.

AT1. Sample directional results, p. 23.

All of the postcruise samples, as well as all shipboard samples from Site 1267, were either alternating-field (AF) or thermally demagnetized. Based on the results of these samples, only some of the remaining coarsely spaced shipboard samples were demagnetized. Most samples were AF demagnetized in steps up to 40 or 60 mT. For AF fields ≥30 mT, we used the "double-demagnetization" technique (Tauxe et al., 1995)

because samples tend to acquire a spurious magnetization in the direction of the alternating field. A few high-coercivity samples were demagnetized up to 180 mT.

Twelve samples from Hole 1267A (across the hypothesized C24r/C24n boundary) were instead subjected to thermal demagnetization. Samples were dried inside a magnetically shielded room, removed from their plastic cubes, and wrapped in aluminum foil. Natural remanent magnetization (NRM) directions for these dried samples are well grouped and statistically indistinguishable from samples measured wet from the same interval. Dried samples were heated in 50°C steps up to 550°C and then additionally at 575°C. Bulk susceptibility was measured between heating steps in an attempt to monitor sample alteration.

One sample from each core from Hole 1267A was subjected to further analysis in the form of the Lowrie three-axis isothermal remanent magnetization (IRM) experiment (Lowrie, 1990). A saturation IRM was acquired in steps, with a maximum applied field of 2.0 T. One exception was Sample 208-1267A-8H-4, 88 cm (0712), where the maximum field was 2.5 T. This saturation IRM, followed by IRMs of 0.3 and 0.1 T, were applied in three orthogonal directions in order to separate the high-, intermediate-, and low-coercivity spectra. The samples were then thermally demagnetized to provide information on the blocking temperature spectra of the various coercivity fractions. A small amount of material from these same samples was reserved for hysteresis measurements, which were carried out on a Princeton Measurements Corp. MicroMag Model 2900 Alternating Gradient Force magnetometer with a maximum applied field of 1 T.

RESULTS

Directional Data

A large (~50%–80% of the NRM) vertical drilling overprint was typically removed by 15 mT or 200°C (Figs. **F2, F3**). The remaining remanence decays to the origin of a vector endpoint diagram for most samples. The AF demagnetized samples, however, often appear to acquire a remanence at steps >40 mT that is not compensated for by the double-demagnetization procedures. This typically occurs when the remanence is less than a few percent of the NRM, and we disregard these steps in the calculation of a principal component. Results from thermally demagnetized samples are consistent with those from AF demagnetized samples (Fig. **F3**).

The remanence direction was calculated by principal component analysis (Kirschvink, 1980) for steps from 15 to 40 mT (five to seven points) for most samples. A few higher coercivity samples (e.g., Fig. **F2B**) were calculated at higher levels. Directions with a maximum angular deviation (Kirschvink, 1980) >15° (e.g., Fig. **F2H**) or samples that did not decay to the origin of the vector endpoint diagram (e.g., Fig. **F2G**) were rejected. The remaining inclinations were used, along with shipboard pass-through data, to determine polarity.

In most, but not all cases, the discrete sample inclination agreed in polarity with the pass-through data, but often provided a less ambiguous answer (Figs. **F4, F5**). See, for example, results from Chron C28r in Hole 1262C at ~210 meters composite depth (mcd), or Chron C23 at ~100–118 mcd (Fig. **F4**). Declination data suffer from bias (Fig. **F6**), though perhaps not to the same degree as the shipboard data (Zachos,

F2. AF demagnetization results, p. 10.

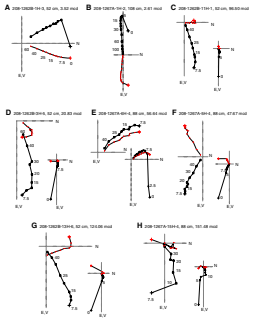

F3. Thermal and AF demagnetization results, p. 11.

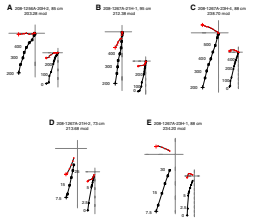

F4. Magnetostratigraphy, Site 1262, p. 12.

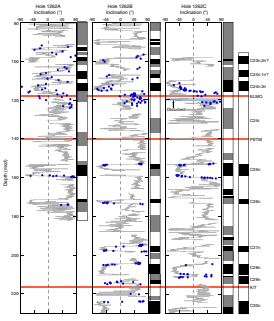

F5. Magnetostratigraphy, Site 1267, p. 13.

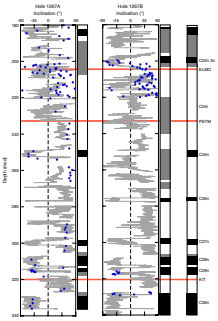

Kroon, Blum, et al., 2004). Whereas the shipboard declinations from archive halves clustered around 0° in core coordinates, the discrete sample declinations from working halves tend to cluster around 180° (Fig. F6). This suggests some kind of radial overprint (e.g., Fuller et al., 1998). Because the declinations do not appear to provide meaningful results, we will focus discussion on the inclination data.

Inclination data remain quite scattered above the P/E boundary; below the boundary, scatter is suppressed, as in the pass-through cryomagnetometer data, and many of the data seem to cluster around the expected GAD value of 53°–56°. However, some inclinations appear excessively steep and may be related to an incompletely removed vertical drilling overprint.

Over the critical C24r/C24n boundary at Site 1262 (Fig. F4), the discrete sample inclinations show significant scatter, yet all three holes show a transition from reversed to normal polarity at ~115–116 mcd. This significant revision to the shipboard interpretation, which placed the boundary at ~120 mcd, was reported in Lourens et al. (2005). The discrete samples also allowed identification of this same boundary at Site 1267 (~201–207 mcd), although with less precision (Fig. F5). At Site 1266, the discrete sample inclinations were highly scattered and did nothing to help identify the C24r/C24n boundary.

At several boundaries in the Paleocene or Late Cretaceous, discrete samples resolved some ambiguities and allowed us to constrain most reversals to within ~10–30 cm at Sites 1262 and 1267. However, for the upper parts of the cores, the coarsely spaced sampling did not significantly resolve any magnetostratigraphic issues, and we do not plot these data. Principal components for all discrete samples are listed in the Table AT1. Tables T1, T2, T3, T4, T5, and T6 list all magnetostratigraphic picks and highlight boundaries that are new or changed from the Leg 208 *Initial Reports* volume (Zachos, Kroon, Blum, et al., 2004).

Rock Magnetic Results

Hysteresis data were difficult to obtain on the weakly magnetized, carbonate-rich sediments. After removing the predominant diamagnetic signal, a few relatively noise free loops were obtained. Hysteresis parameters are summarized in a typical Day plot (Day et al., 1977) in Figure F7A and are reflective of multidomain (MD) to pseudo-single-domain size grains. Alternatively, on a squareness (M_r/M_s) vs. coercivity plot as in Tauxe et al. (2002), samples plot on a mixing trend between MD and vortex-state grains (Fig. F7B).

Results from the Lowrie three-axis IRM experiments can be summarized as being of three different types (Fig. F8). Type 1 sediments (Fig. F8A) are found above ~98 mcd in Hole 1267A and are characterized by a large soft (≤0.1 T) component that shows a partial unblocking at ~150°–200°C but otherwise decays with nearly constant slope to zero between 550° and 600°C. Minor medium and hard fractions also decay consistently to zero at 550°–600°C. These results are consistent with coarse-grained magnetite mixed with titanomagnetite. However, one sample of this type (Sample 208-1267A-1H-3, 108 cm [0663]) has slightly larger medium and hard components (combined ~25% of the total), which also show evidence for partial unblocking at ~250°C (Fig. F8B). It is possible that these hard components represent a contribution from pyrrhotite or greigite, although reported maximum unblocking temperatures are somewhat higher for these minerals at 325° and 333°C, respectively (Dekkers, 1989; Roberts, 1995).

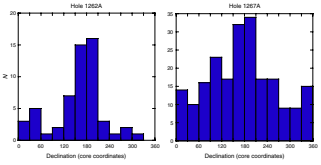

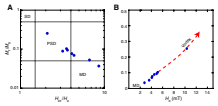

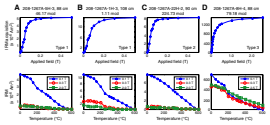

The coercivity of remanence derived from the hysteresis loops for all samples is low (14–24 mT), which is more consistent with a hysteresis dominated by (titano)magnetite rather than greigite or pyrrhotite (Roberts, 1995; Peters and Dekkers, 2003). The ratio of saturation IRM to low-field susceptibility has been suggested as a way to discriminate among several magnetic remanence carriers (e.g., Peters and Dekkers, 2003). Greigite and pyrrhotite typically have higher values than titanomagnetite, but the fields for the three minerals do overlap. Calculated values for this ratio are slightly higher for the Type 1 sediments (average = 25.2 kA/m) compared to the Type 2 sediments (average = 12.9 kA/m). Although the higher Type 1 values fall within the lower range of both pyrrhotite and greigite, all values still fall within the range for titanomagnetite.

To further explore the possible presence of iron sulfides in the medium or hard components, a few magnetic grains were separated from the noncarbonate fraction for scanning electron microscopy (SEM) analysis (Samples 208-1267A-1H-4, 108 cm, and 1H-5, 108 cm [0664 and 0665]). Results from two grains are consistent with titanomagnetite ($Fe_{3-x}Ti_xO_4$) with x being ~0.49 and ~0.35, respectively. Titanomagnetites with these compositions correspond to Curie temperatures ranging from ~250° to 350°C. Al and Mg impurities are also present, however, and will lower T_c somewhat (Dunlop and Özdemir, 1997). Although we cannot definitively exclude the presence of iron sulfides in these samples, it seems likely that titanomagnetite can explain the unblocking at 250°C, although coercivities as high as 0.3 T would be unusual.

Type 2 sediments (Fig. **F8C**) are very similar to Type 1 sediments but show no evidence for the low-temperature unblocking of the soft component. These sediments, therefore, contain predominately coarse grained magnetite and are lacking the titanomagnetite inferred to be present in the Type 1 sediments. Type 2 sediments are found below ~98 mcd, although two samples with profiles intermediate between Types 1 and 2 are found between 98 and 129 mcd and another is found at ~264 mcd.

Type 3 sediments are represented by Sample 208-1267A-8H-4, 88 cm (0712) (Fig. **F8D**), found in an interval of extremely low remanent intensity and susceptibility at ~70–83 mcd at Site 1267 (see figs. F21 and F22 of Chapter 8 in Shipboard Scientific Party, 2004). This sample has the same low-coercivity behavior as Type 1 but also has large medium- and high-coercivity fractions that are not completely demagnetized by 600°C. This is consistent with a large contribution from hematite, as well as magnetite and titanomagnetite.

The downhole transition from Type 1 to Type 2 sediments is accompanied by an increase in remanent intensity and a decrease in the average median destructive field. This change to lower coercivity sediments below ~98 mcd can also be seen in the pass-through data by calculating the fraction of the NRM removed by demagnetization to 15 mT. These same changes in coercivity and intensity can be observed at all sites in the pass-through data at the same stratigraphic horizon in the upper Miocene. At Sites 1262 and 1267, this horizon has also been characterized as the transition between lithostratigraphic Units I and II. In several holes, the horizon roughly correlates with local pore water maximums in Mn^{2+} and minimums in Fe^{2+} (e.g., fig. F1 of Chapter 8 in Shipboard Scientific Party, 2004), suggesting a possible diagenetic link to redox conditions that might precipitate iron sulfides. However, because of the local nature of these peaks, we suggest the consistent presence of Type 1 sediments above the upper Miocene horizon is reflective

of a change in the source of the detrital grains (magnetite/titanomagnetite) at this time.

CONCLUSIONS

The discrete sample analyses result in the following major conclusions:

1. Directional data obtained from the discrete samples do not, in most cases, provide a significant improvement over the pass-through data. However, in some cases these new data were able to resolve ambiguities in the magnetostratigraphic record.
2. Significantly, the C24r/C24n reversal boundary was identified at Sites 1262 and 1267, and most boundaries in the Paleocene and Upper Cretaceous sections are now identified to within 10–30 cm.
3. Magnetic mineralogy results show that prior to the late Miocene, the predominant detrital magnetic component was coarse-grained magnetite and that after the late Miocene titanomagnetite has also been present. This suggests a possible change in detrital source at that time.

ACKNOWLEDGMENTS

This work benefited from many helpful discussions with Lisa Tauxe, Jeff Gee, and Thomas Westerfold. Stefanie Brachfeld provided a very constructive review that helped improve the manuscript. The author would also like to thank the scientists, staff, and crew of Leg 208. Special thanks go to Lauren Kay for assistance with many measurements. This research used samples and data provided by the Ocean Drilling Program (ODP). ODP is sponsored by the U.S. National Science Foundation (NSF) and participating countries under management of Joint Oceanographic Institutions (JOI), Inc. Funding for this research was provided by the U.S. Science Support Program.

REFERENCES

Cande, S.C., and Kent, D.V., 1995. Revised calibration of the geomagnetic polarity timescale for the Late Cretaceous and Cenozoic. *J. Geophys. Res.,* 100(B4):6093–6095. **doi:10.1029/94JB03098**

Day, R., Fuller, M., and Schmidt, V.A., 1977. Hysteresis properties of titanomagnetites: grain-size and compositional dependence. *Phys. Earth Planet. Inter.,* 13:260–267.

Dekkers, M.J., 1989. Magnetic properties of natural goethite, Part II. TRM behaviour during thermal and alternating field demagnetization and low-temperature treatment. *Geophys. J. R. Astron. Soc.,* 97:341–355.

Dunlop, D.J., and Özdemir, Ö., 1997. *Rock Magnetism: Fundamentals and Frontiers:* Cambridge (Cambridge Univ. Press).

Fuller, M., Hastedt, M., and Herr, B., 1998. Coring-induced magnetization of recovered sediment. *In* Weaver, P.P.E., Schmincke, H.-U., Firth, J.V., and Duffield, W. (Eds.), *Proc. ODP, Sci. Results,* 157: College Station, TX (Ocean Drilling Program), 47–56. [**PDF**]

Kirschvink, J.L., 1980. The least-squares line and plane and the analysis of palaeomagnetic data. *Geophys. J. R. Astron. Soc.,* 62(3):699–718.

Lourens, L.J., Hilgen, F.J., Laskar, J., Shackleton, N.J., and Wilson, D., 2004. The Neogene period. *In* Gradstein, F.M., Ogg, J., et al. (Eds.), *A Geologic Time Scale 2004:* Cambridge (Cambridge Univ. Press).

Lourens, L.J., Sluijs, A., Kroon, D., Zachos, J.C., Thomas, E., Röhl, U., Bowles, J., and Raffi, I., 2005. Astronomical pacing of late Palaeocene to early Eocene global warming events. *Nature (London, U. K.),* 435(7045):1083–1087. **doi:10.1038/nature03814**

Lowrie, W., 1990. Identification of ferromagnetic minerals in a rock by coercivity and unblocking temperature properties. *Geophys. Res. Lett.,* 17:159–162.

O'Connor, J.M., and Duncan, R.A., 1990. Evolution of the Walvis Ridge–Rio Grande Rise hotspot system: implications for African and South American Plate motions over plumes. *J. Geophys. Res.,* 95:17475–17502.

Peters, C., and Dekkers, M., 2003. Selected room-temperature magnetic parameters as a function of mineralogy, concentration and grain size. *Phys. Chem. Earth,* 28:659–667. **doi:10.1016/S1474-7065(03)00120-7**

Roberts, A.P., 1995. Magnetic properties of sedimentary greigite (Fe_3S_4). *Earth Planet. Sci. Lett.,* 134:227–236. **doi:10.1016/0012-821X(95)00131-U**

Shipboard Scientific Party, 2004. Site 1267. *In* Zachos, J.C., Kroon, D., Blum, P., et al., *Proc. ODP, Init. Repts.,* 208: College Station, TX (Ocean Drilling Program), 1–77. **doi:10.2973/odp.proc.ir.208.108.2004**

Smith, W.H.F., and Sandwell, D.T., 1997. Global seafloor topography from satellite altimetry and ship depth soundings. *Science,* 277:1956–1962. **doi:10.1126/science.277.5334.1956**

Tauxe, L., Bertram, H.N., and Seberino, C., 2002. Physical interpretation of hysteresis loops: micromagnetic modeling of fine particle magnetite. *Geochem., Geophys., Geosyst.,* 3(10):1055. **doi:10.1029/2001GC000241**

Tauxe, L., Pick, T., and Kok, Y.S., 1995. Relative paleointensity in sediments: a pseudo-Thellier approach. *Geophys. Res. Lett.,* 22(21):2885–2888. **doi:10.1029/95GL03166**

Zachos, J.C., Kroon, D., Blum, P., et al., 2004. *Proc. ODP, Init. Repts.,* 208: College Station, TX (Ocean Drilling Program). **doi:10.2973/odp.proc.ir.208.2004**

APPENDIX

See Table AT1 for descrete sample directional results.

Figure F1. ODP Leg 208 sites on Walvis Ridge. Data from Sites 1262 and 1267 are discussed in detail in the text. Bathymetry data from Smith and Sandwell (1997).

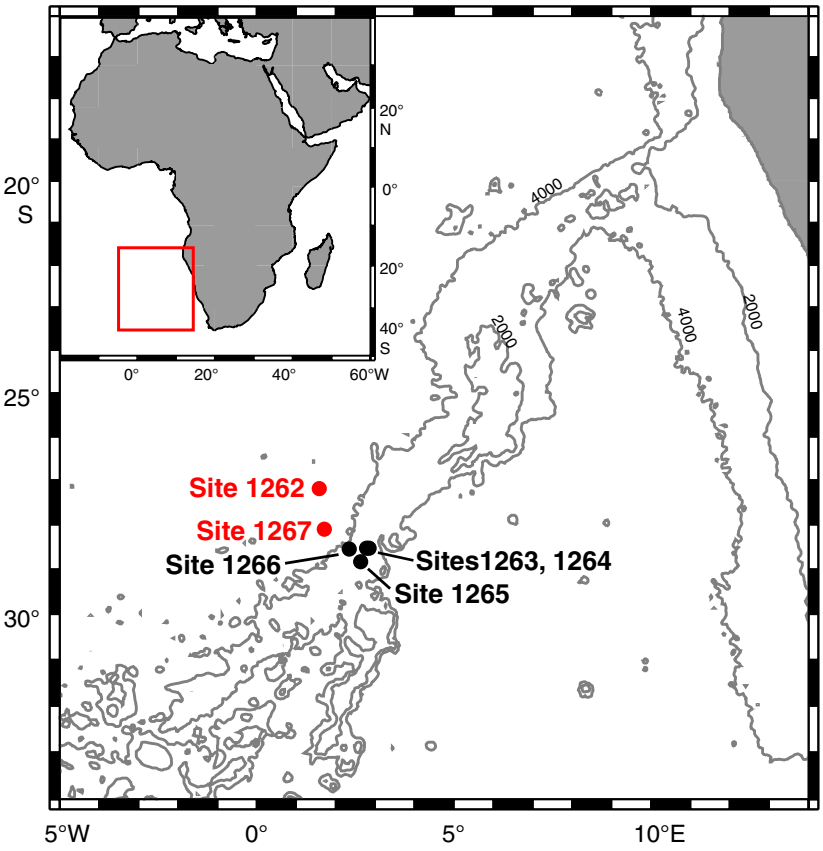

Figure F2. A–F. Representative vector endpoint diagrams from AF demagnetization. Horizontal projection shown with solid red dots, vertical projection shown with open squares. Demagnetization steps shown in milliTeslas. A vertical drilling overprint is typically removed by 15 mT. When this overprint is very large, the smaller, complete diagram is shown to the right, and steps ≥7.5 mT are shown at full size to the left. These examples are typical of samples used to determine polarity. Samples that did not decay to the origin (G) and samples with excessively high maximum angular deviation values (H) were not used.

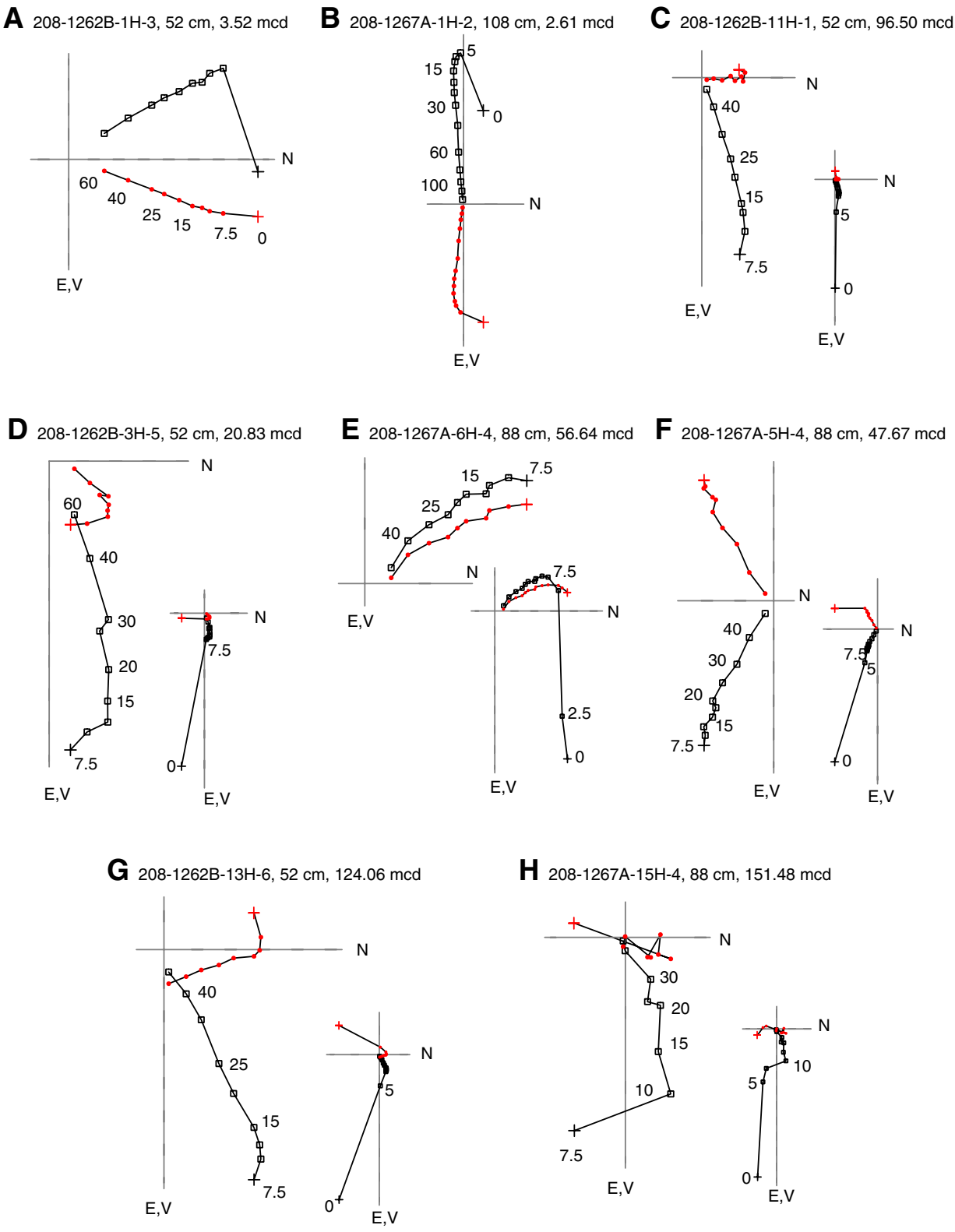

Figure F3. A–C. Representative vector endpoint diagrams from thermal demagnetizations. Horizontal projection shown with solid red dots, vertical projection shown with open squares. Temperature steps indicated in degrees Celsius. **D, E.** AF demagnetization results from adjacent samples for comparison. Demagnetization steps are shown in mT.

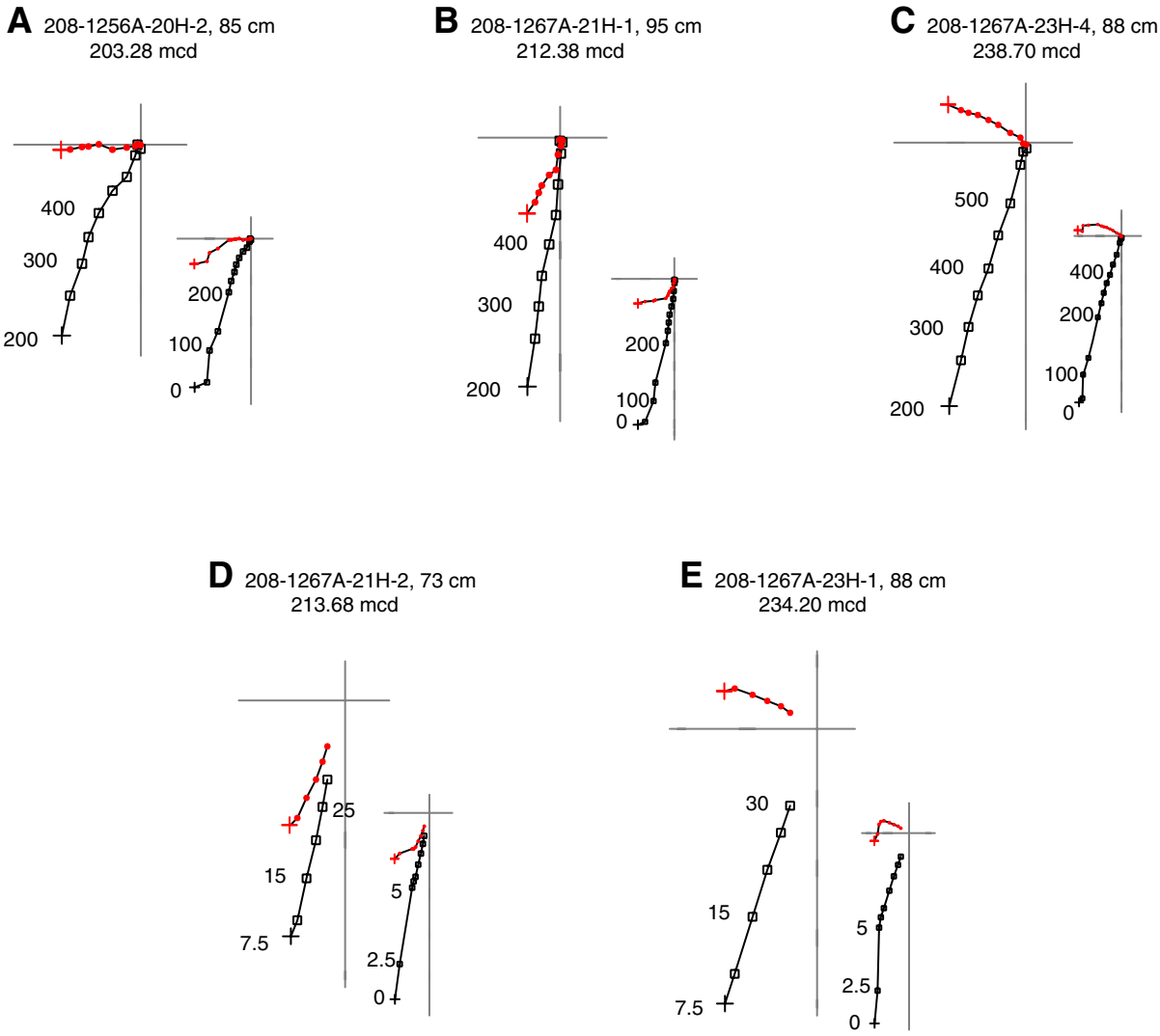

Figure F4. Upper Cretaceous to lower Eocene magnetostratigraphy for Site 1262. Shipboard pass-through inclination (demagnetized to 15 mT; gray lines) and discrete sample inclination (principle component calculated as in text; blue circles) are shown. Shaded interval in Hole 1262C represents a particularly disturbed core section, results from which should not be considered reliable. Overall magnetostratigraphic interpretation on the right; black = normal polarity, white = reverse polarity, gray = indeterminate polarity. PETM = Paleocene/Eocene Thermal Maximum, K/T = Cretaceous/Tertiary boundary.

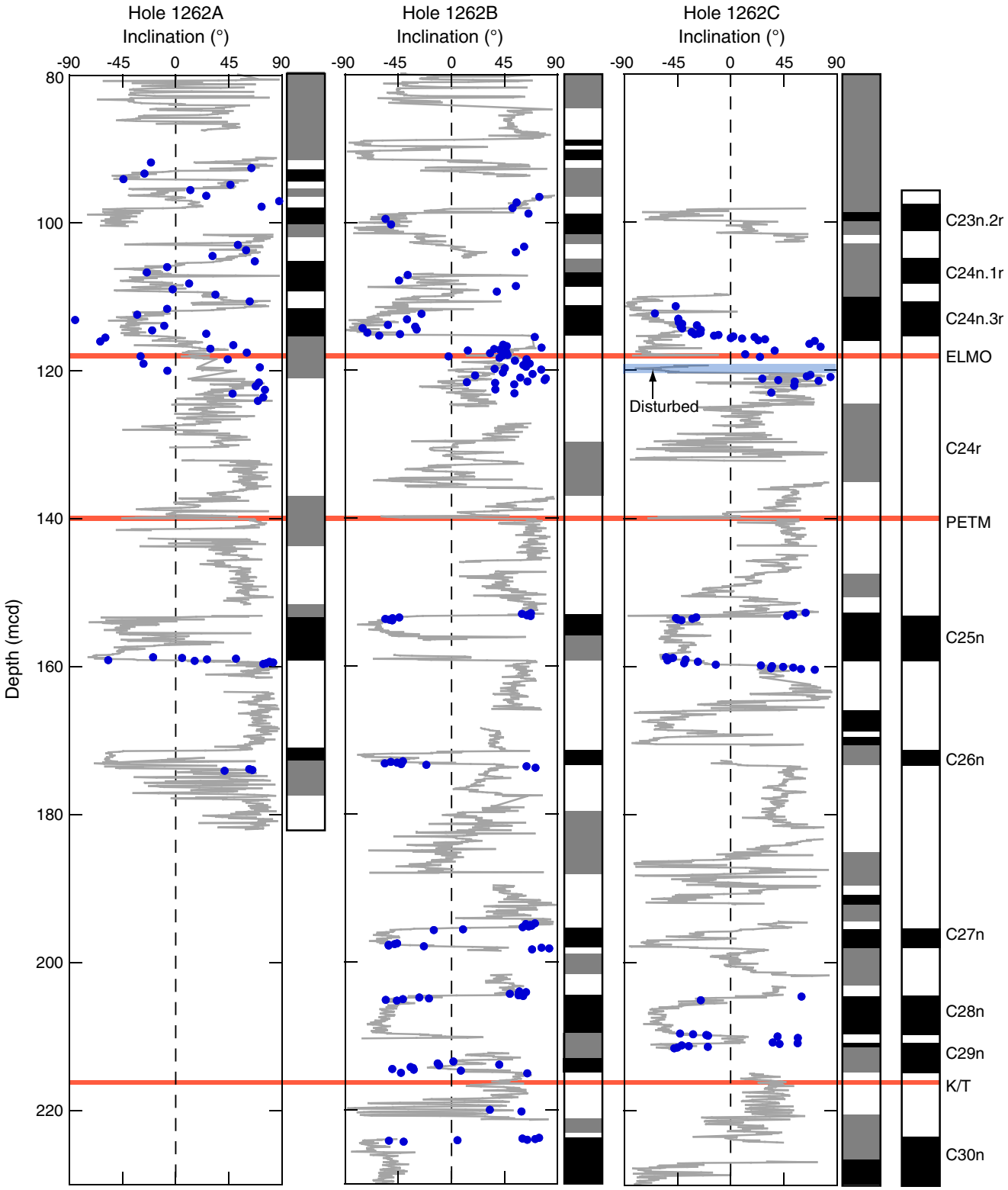

Figure F5. Upper Cretaceous to lower Eocene magnetostratigraphy for Site 1267. Shipboard pass-through inclination (demagnetized to 15 mT; gray lines) and discrete sample inclination (principal component calculated as in text; blue circles) are shown. Overall magnetostratigraphic interpretation on the right; black = normal polarity, white = reverse polarity, gray = indeterminate polarity. PETM = Paleocene/Eocene Thermal Maximum, K/T = Cretaceous/Tertiary boundary.

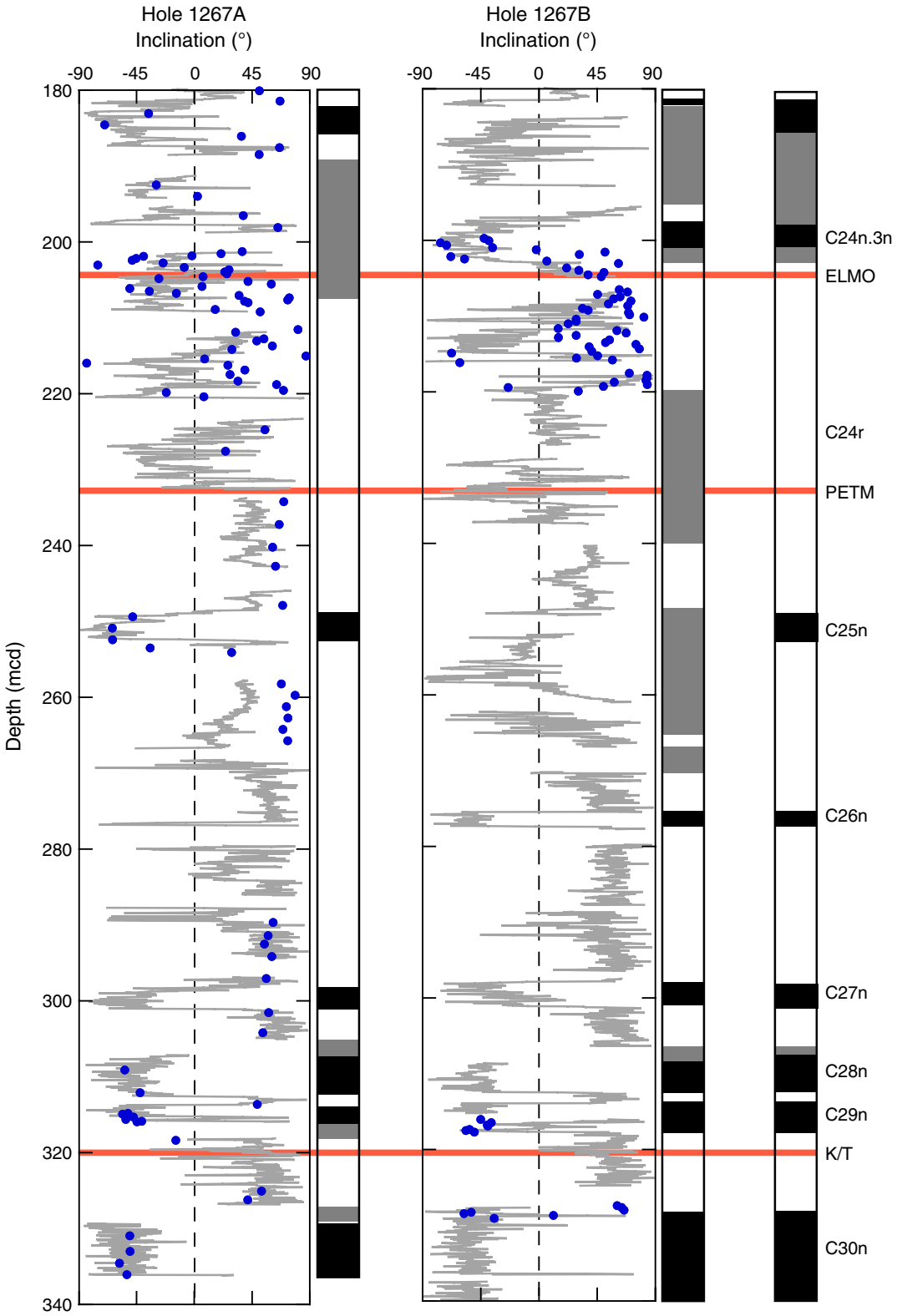

Figure F6. Histograms of discrete sample declinations for Holes 1262A and 1267A. Declinations in core coordinates (i.e., unoriented with respect to north) show a bias toward 180°.

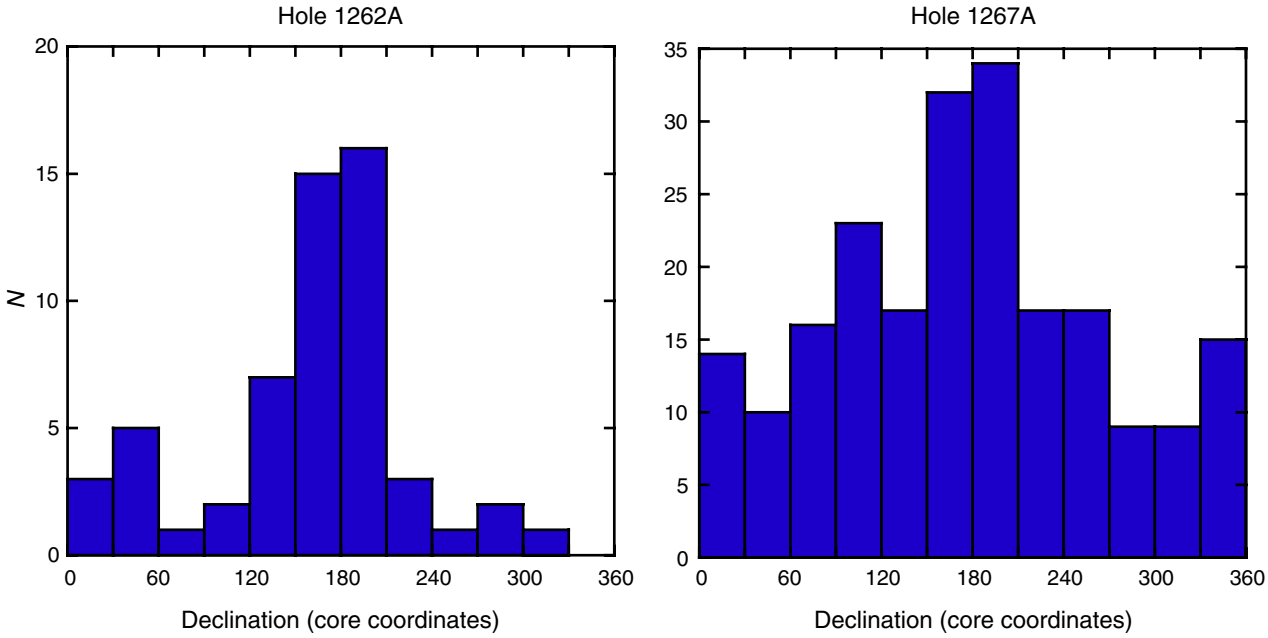

Figure F7. Hysteresis parameters of samples from Hole 1267A. **A.** Results plotted on a typical Day diagram fall predominantly in the pseudo-single-domain (PSD) to multidomain (MD) regions. **B.** The same data plotted as squareness (M_r/M_s) vs. H_c as in Tauxe et al. (2002) show that samples plot along a mixing line between MD and the vortex state that is transitional to single domain (SD).

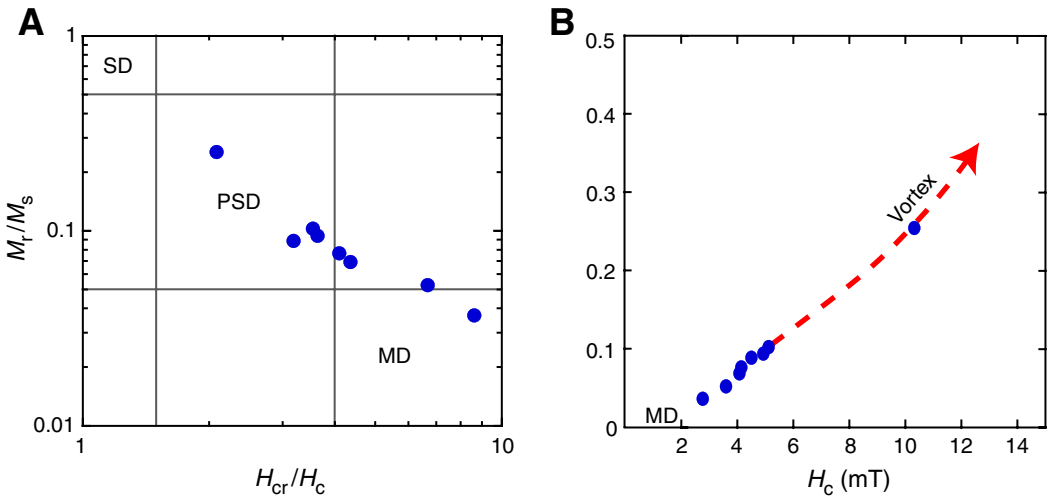

Figure F8. Typical results from isothermal remanent magnetization (IRM) acquisition and Lowrie three-axis IRM tests (Lowrie, 1990). **A, B.** Type 1 samples are found above ~98 mcd in Hole 1267A and results are consistent with a mixture of titanomagnetite and coarse-grained magnetite. **C.** Type 2 sediments are found below ~98 mcd and are consistent with predominantly coarse-grained magnetite only. **D.** Type 3 sediments are found between ~70 and 83 mcd and are consistent with a mixture of titanomagnetite, coarse-grained magnetite, and hematite.

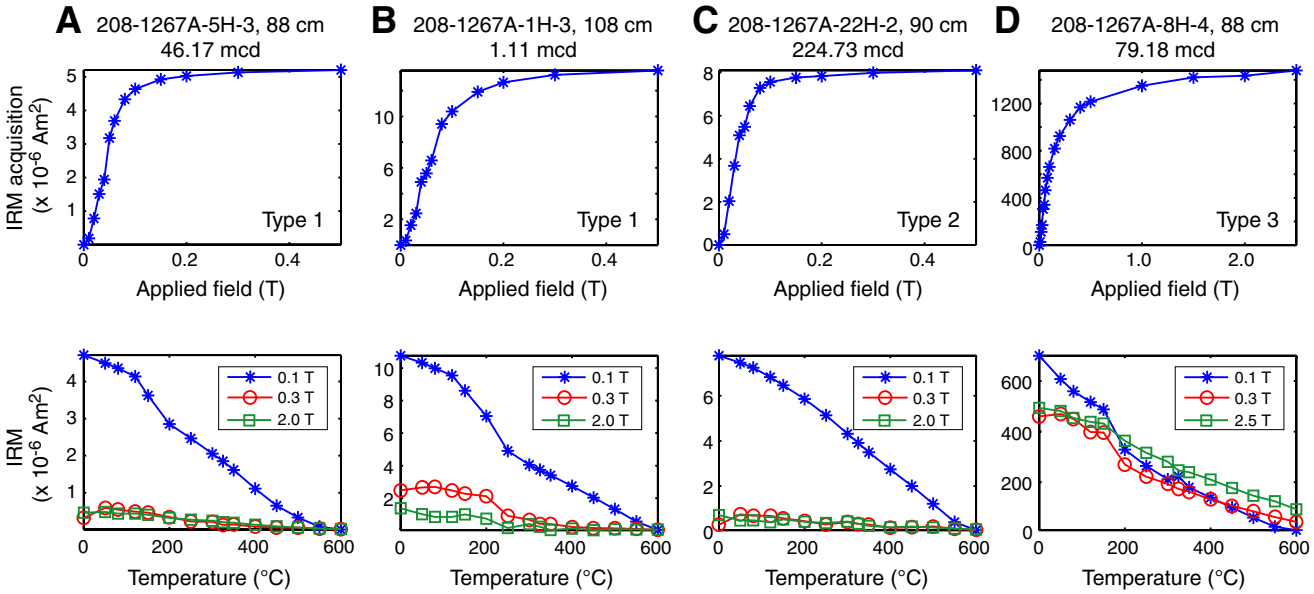

Table T1. Magnetostratigraphic age-depth tie points, Site 1262.

Chron	Age (Ma)		Top				Bottom			
	Lourens et al. (2004)	Cande and Kent (1995)	Hole	Section, interval (cm)	Depth (mbsf)	Depth (mcd)	Hole	Section, interval (cm)	Depth (mbsf)	Depth (mcd)
C1n (o)	0.781	0.78	1262B	1H-5, 15	6.15	6.15	1262B	2H-2, 140	9.8	6.47
C1r.1n (t)	0.988	0.99		2H-2, 140	9.8	7.44	1262A	1H-2, 5	1.55	7.59
C1r.1n (o)	1.072	1.07	1262A	1H-2, 45	1.95	7.99	1262B	2H-4, 10	11.5	8.17
Cobb Mountain (t)	1.173	1.201		1H-2, 135	2.85	8.89		2H-2, 100	12.4	9.07
Cobb Mountain (o)	1.185	1.211		1H-3, 5	3.05	9.09		2H-4, 135	12.75	9.42
C2n (t)	1.785	1.77	1262B	3H-1, 115	13.05	15.46		3H-1, 125	15.56	15.56
C2n (o)	1.942	1.95		3H-2, 105	14.45	16.86		3H-2, 115	14.55	16.96
C21262An.1n (t)	2.582	2.581	1262A	2H-6, 90	17.87	24.18		4H-1, 100	22.4	24.39
C13n (t)	33.058	33.058		9H-2, 90	69.8	76.67	1262A	7H-6, 125	65.75	77.14
C13n (o)	33.545	33.545		9H-4, 15	72.05	78.92	1262B	9H-4, 125	72.2	79.07
C23n (o)*	51.743	51.743		11H-3, 27	90.67	100.25		11H-4, 112	92.02	101.6
C24n.1n (t)*	52.363	52.363	1262A	10H-3, 52	89.02	105.13	1262A	10H-4, 52	90.52	106.63
C24n.1n (o)*	52.663	52.663	1262B	12H-1, 127	97.17	107.81	1262B	12H-2, 52	97.92	108.56
C24n.3n (t)*	52.903	52.903		12H-3, 127	100.17	110.81	1262C	2H-3, 52	101.52	111.31
C24n.3n (o)*	53.347	53.347	1262C	2H-4, 142	105.42	115.21		2H-5, 72	106.22	116.01
C25n (t)*	55.904	55.904	1262B	16H-5, 42	140.32	153.18		7H-1, 122	142.72	153.31
C25n (o)*	56.391	56.391	1262A	15H-4, 142	138.92	159.08		7H-6, 42	149.42	160.01
C26n (t)*	57.554	57.554		16H-6, 44	150.44	171.4	1262B	18H-3, 101	156.91	172
C26n (o)*	57.911	57.911	1262B	18H-4, 72	158.1	173.21		17H-4, 92	158.32	173.41
C27n (t)*	60.92	60.92		20H-5, 2	177.92	195.25		20H-5, 42	178.32	195.65
C27n (o)*	61.276	61.276		20H-6, 102	180.42	197.75		20H-6, 132	180.72	198.05
C28n (t)*	62.499	62.499		21H-3, 122	185.62	204.5		21H-3, 142	185.82	204.76
C28n (o)*	63.634	63.634	1262C	12H-5, 82	190.82	209.6	1262C	12H-5, 112	191.12	209.9
C29n (t)*	63.976	63.976		12H-6, 62	192.12	210.9		12H-6, 82	192.32	211.1
C29n (o)*	64.745	64.745	1262B	22H-3, 75	193.41	214.4	1262B	22H-3, 136	194.02	215.01
C30n (t)*	65.578	65.578		23H-1, 42	200.82	224		23H-1, 57	200.97	224.15

Notes: o = onset, t = termination. Chron C13n (t) and (o) are a lower confidence picks. * = new and/or revised boundaries compared to Leg 208 *Initial Reports* (Zachos, Kroon, Blum, et al., 2004).

Table T2. Magnetostratigraphic age-depth tie points, Site 1263.

Chron	Age (Ma)		Top				Bottom			
	Lourens et al. (2004)	Cande and Kent (1995)	Hole	Section, interval (cm)	Depth (mbsf)	Depth (mcd)	Hole	Section, interval (cm)	Depth (mbsf)	Depth (mcd)
C12n (t)	30.476	30.476	1263A	7H-3, 50	53.3	62.41	1263B	2H-1, 85	56.35	65.76
C12n (o)	30.939	30.939		7H-6, 145	58.75	67.86	1263A	8H-1, 55	59.85	70.56
C13n (t)	33.058	33.058		9H-3, 5	71.85	83.62	1263B	4H-2, 5	76.05	88.14
C13n (o)	33.545	33.545		9H-7, 35	77.65	89.42		4H-4, 65	79.65	91.74
C19n (t)	41.257	41.257	1263B	9H-4, 135	127.85	147.8	1263A	15H-2, 40	127.7	148.22
C19n (o)	41.521	41.521		9H-5, 125	129.25	149.2		15H-3, 50	129.3	149.82

Notes: o = onset, t = termination. All boundaries are lower confidence picks.

Table T3. Magnetostratigraphic age-depth tie points, Site 1264.

Chron	Age (Ma)		Top				Bottom			
	Lourens et al. (2004)	Cande and Kent (1995)	Hole	Section, interval (cm)	Depth (mbsf)	Depth (mcd)	Hole	Section, interval (cm)	Depth (mbsf)	Depth (mcd)
C2n (t)	1.785	1.77	1264A	1H-5, 140	7.4	10.36	1264B	2H-2, 135	10.15	11.26
C2An (t)	2.582	2.581		2H-2, 125	12.05	16.38	1264A	2H-4, 25	14.05	18.38
C2An (o)	3.596	3.58	1264B	3H-2, 130	24.68	27.49		3H-5, 60	25.4	31.29
C3n (t)	4.188	4.18		4H-3, 100	30.3	33.75	1264B	4H-3, 145	30.75	34.2

Notes: o = onset, t = termination. All boundaries are lower confidence picks.

Table T4. Magnetostratigraphic age-depth tie points, Site 1265.

Chron	Age (Ma)		Top				Bottom			
	Lourens et al. (2004)	Cande and Kent (1995)	Hole	Section, interval (cm)	Depth (mbsf)	Depth (mcd)	Hole	Section, interval (cm)	Depth (mbsf)	Depth (mcd)
C1n (o)	0.781	0.780	1265B	1H-3, 85	3.68	3.67	1265B	1H-4, 20	4.03	4.02
C2n (t)	1.785	1.770	1265A	1H-5, 30	6.30	7.92	1265A	1H-6, 25	7.75	9.37
C2n (o)	1.942	1.950		1H-7, 15	9.15	10.77		2H-1, 60	10.10	12.83
C5En (o)	18.524	18.781		9H-2, 90	78.40	89.52		9H-2, 135	78.85	89.97
C6n (t)	18.748	19.048		9H-2, 140	78.90	90.02		9H-3, 65	79.65	90.77
C6n (o)	19.722	20.131		9H-7, 40	84.90	96.02		10H-1, 60	86.10	98.17
C6An (t)	20.040	20.518		10H-2, 90	87.90	99.97		10H-3, 30	88.80	100.87
C6An (o)	20.709	20.320		10H-6, 25	93.25	105.32		10H-6, 80	93.80	105.87
C6Bn (t)	21.767	22.588		11H-3, 45	98.45	112.22		11H-3, 145	99.45	113.22
C6Bn (o)	22.268	23.069		11H-7, 45	104.45	118.22	1265B	12H-4, 35	104.52	118.97
C6Cn.1n (t)*	22.564	23.353	1265B	12H-5, 128	106.95	121.40	1265A	12H-2, 64	106.64	121.60
C6Cn.1n (o)*	22.754	23.535	1265A	12H-2, 128	107.28	122.24		12H-3, 8	107.58	122.54
C6Cn.2n (t)	22.902	23.677		12H-3, 140	108.90	123.86		12H-4, 40	109.40	124.36
C6Cn.2n (o)*	23.030	23.800		12H-4, 78	109.78	124.74		12H-4, 93	109.93	124.89
C6Cn.3n (t)*	23.230	23.999		12H-5, 58	111.08	126.04		12H-5, 79	111.29	126.25
C6Cn.3n (o)*	23.340	24.118		12H-5, 118	111.68	126.64		12H-5, 138	111.88	126.84
C7n (t)	24.011	24.730		13H-3, 5	117.05	132.95		13H-4, 105	119.55	135.45
C13n (t)	33.058	33.058		18H-3, 20	164.70	186.70		18H-3, 55	165.05	187.05
C13n (o)	33.545	33.545	1265B	18H-7, 25	165.95	188.48		18H-7, 5	169.03	191.13
C25n (t)	55.904	55.904	1265A	32H-4, 140	284.10	325.83		32H-5, 10	284.30	326.03

Notes: o = onset, t = termination. Chrons C1n–C12n are lower confidence picks. * = new and/or revised boundary compared to Leg 208 *Initial Reports* (Zachos, Kroon, Blum, et al., 2004).

Table T5. Magnetostratigraphic age-depth tie points, Site 1266.

Chron	Age (Ma)		Top				Bottom			
	Lourens et al. (2004)	Cande and Kent (1995)	Hole	Section, interval (cm)	Depth (mbsf)	Depth (mcd)	Hole	Section, interval (cm)	Depth (mbsf)	Depth (mcd)
C1n (o)	0.781	0.78	1266A	1H-3, 50	3.50	6.64	1266A	1H-4, 10	4.60	7.74
C1r.1n (t)	0.988	0.99		1H-4, 20	4.70	7.84		1H-4, 90	5.40	8.54
C1r.1n (o)	1.072	1.07		1H-5, 45	6.45	9.59		1H-5, 110	7.10	10.24
C2n (t)	1.785	1.77		2H-3, 85	13.35	17.92		2H-3, 130	13.80	18.37
C2n (o)	1.942	1.95		2H-5, 80	16.30	20.87		2H-5, 105	16.55	21.12
C2An (t)	2.582	2.581		3H-2, 40	20.90	26.89		3H-4, 5	23.55	29.54
C3n (o)	5.236	5.23		6H-7, 65	57.15	67.42		7H-1, 70	57.70	69.39
C5n (o)	11.043	10.949		9H-3, 30	79.30	93.84		9H-4, 20	80.70	95.24
C6Cn (t)	22.564	23.353		13H-4, 95	118.55	138.65		13H-5, 10	119.20	139.30
C7n (o)*	24.451	25.183		14H-6, 92	131.02	152.55		14H-6, 102	131.12	152.65
C7An (t)	24.781	25.496	1266C	9H-1, 95	135.95	154.43	1266C	9H-1, 115	136.15	154.63
C7An (o)	24.942	25.648		9H-2, 45	136.95	155.43		9H-2, 85	137.35	155.83
C8n (t)	25.053	25.823		9H-2, 145	137.95	156.5		9H-4, 25	139.75	158.23
C10n (t)	27.76	28.283	1266A	17H-2, 110	153.70	179.51	1266A	17H-2, 120	153.80	179.61
C10n (o)	28.053	28.745	1266C	11H-6, 20	162.70	184.06		17H-7, 55	160.15	185.96
C11n (o)	29.828	30.098	1266A	18H-3, 45	164.05	191.28	1266C	12H-3, 140	167.90	191.63
C12n (t)	30.479	30.479	1266C	12H-4, 110	169.10	192.83	1266A	18H-5, 40	167.00	194.23
C12n (o)	30.939	30.939		12H-5, 95	170.45	194.18		18H-6, 10	168.20	195.43
C13n (t)	33.058	33.058		13H-7, 20	182.20	207.67		20H-1, 100	180.60	210.68
C15n (t)	34.655	34.655	1266A	21H-3, 30	192.40	223.9		21H-3, 50	192.60	224.10
C15n (o)	34.94	34.94		21H-3, 145	193.55	225.05		21H-4, 20	193.80	225.30
C16n (t)	35.343	35.343		21H-4, 105	194.65	226.15		21H-5, 40	195.50	227.00
C26n (o)	57.911	57.911	1266C	20X-3, 5	318.05	364.33	1266B	12X-4, 45	316.35	364.84

Notes: o = onset, t = termination. Chrons C1n–C12n are lower confidence picks. * = new and/or revised boundary compared to Leg 208 *Initial Reports* (Zachos, Kroon, Blum, et al., 2004).

Table T6. Magnetostratigraphic age-depth tie points, Site 1267.

Chron	Age (Ma)		Top				Bottom			
	Lourens et al. (2004)	Cande and Kent (1995)	Hole	Section, interval (cm)	Depth (mbsf)	Depth (mcd)	Hole	Section, interval (cm)	Depth (mbsf)	Depth (mcd)
C1n (o)*	0.781	0.780	1267B	2H-2, 125	5.85	6.78	1267A	1H-5, 108	7.08	7.11
C1r.1n (t)	0.988	0.990		2H-3, 145	7.55	8.48	1267B	2H-4, 25	7.85	8.78
C1r.1n (o)	1.072	1.070		2H-4,95	8.55	9.48		2H-5, 5	9.15	10.08
C2n (t)	1.785	1.770	1267A	2H-6, 40	16.80	17.47		3H-2, 120	15.30	18.04
C2n (o)	1.942	1.950	1267B	3H-3, 110	16.70	19.44		3H-4, 5	17.15	19.89
C12n (t)	30.479	30.479		13H-3,130	111.90	123.87		13H-4, 65	112.70	124.67
C12n (o)	30.939	30.939		13H-4,105	113.10	125.07		13H-4, 115	113.20	125.17
C13n (t)	33.058	33.058		14H-5,90	123.96	137.43	1267A	14H-2, 30	124.70	137.85
C13n (o)	33.545	33.545	1267A	14H-4,142	128.82	141.97		14H-5, 22	129.12	142.27
C15n (t)*	34.655	34.655		14H-6,70	131.10	144.25		14H-6, 88	131.28	144.43
C15n (o)*	34.940	34.940		14H-6,88	131.28	144.43		14H-6, 115	131.55	144.70
C16n (t)*	35.343	35.343		14H-6,125	131.65	144.80	1267B	15H-3, 119	130.79	145.20
C20n (t)	42.536	42.536	1267B	16H-1,65	136.75	152.13	1267A	15H-5, 100	139.40	153.10
C20n (o)	43.789	43.789		16H-2,105	138.65	154.03		15H-6, 95	140.85	154.55
C21n (t)	46.264	46.264	1267A	16H-3, 60	145.50	161.90		16H-4, 25	146.65	163.05
C24n (o)*	53.347	53.347	1267B	20H-5.8	180.18	200.92		20H-5, 8	185.98	207.03
C25n (t)*	55.904	55.904	1267A	24H-3, 15	221.05	248.64		24H-3, 88	221.78	249.37
C25n (o)*	56.391	56.391		24H-5, 88	244.78	252.37		24H-CC, 38	226.48	254.07
C26n (t)	57.554	57.554	1267B	27X-4, 130	240.20	275.55	1267B	27X-4, 135	240.25	275.60
C26n (o)	57.911	57.911		27X-6, 20	242.10	277.45		27X-6, 30	242.20	277.55
C27n (t)	60.920	60.920		30X-1, 90	264.20	297.94	1267A	29X-2, 105	266.65	298.99
C27n (o)	61.276	61.276		30X-3, 110	267.40	301.14	1267B	30X-3, 140	267.70	301.44
C28n (t)	62.499	62.499		30X-7, 45	272.75	306.49	1267A	30X-1, 75	274.45	307.46
C28n (o)	63.634	63.634		31X-3, 140	277.30	312.55		30X-5, 10	279.80	312.81
C29n (t)	63.976	63.976	1267A	30X-5, 105	280.75	313.76	1267B	31X-4, 140	278.80	314.05
C29n (o)*	64.745	64.745	1267B	32X-2, 58	283.08	317.68		32X-2, 90	283.40	318.00
C30n (t)*	65.578	65.578		33X-1, 73	291.33	327.97		33X-1, 102	291.62	328.26
C30n (o)	67.610	67.610		36X-2, 90	321.80	360.55		36X-2, 100	321.90	360.65
C31n (t)	67.735	67.735		36X-3, 120	323.60	362.35		36X-3, 140	323.80	362.55

Notes: o = onset, t = termination. Chrons C20n (t)–C21n are lower confidence picks. * = new and/or revised boundary compared to Leg 208 *Initial Reports* (Zachos, Kroon, Blum, et al., 2004).

Table AT1. Discrete sample directional results.

Sample number	Core, section (cm)	Depth (mcd)	N	AF demagnetization (mT)		MAD (°)	Declination (°)		Inclination (°)
				Lowest	Highest		Core coordinates	Geographic coordinates	
	208-1262A-								
900	9H-1, 56	91.77	5	15	40	5.1	194.7		–17.3
901	9H-1, 132	92.53	5	15	40	3.8	318.3		63.2
903	9H-2, 56	93.27	5	15	40	2.6	215.7		–26.6
904	9H-2, 131	94.02	5	15	40	4.5	175.2		–41.7
905	9H-3, 56	94.77	5	15	40	5.1	183.7		49.2
906	9H-3, 130	95.51	5	15	40	4.9	169.4		10.8
907	9H-4, 56	96.27	5	15	40	1.3	175.2		24.7
908	9H-4, 130	97.01	5	15	40	3.6	151.6		89.5
909	9H-5, 56	97.77	5	15	40	9.1	180.5		68.6
913	10H-1, 56	102.17	5	15	40	14.1	163.4	326.5	68.6
914	10H-1, 130	102.91	5	15	40	1.7	152.0	315.1	52.8
915	10H-2, 52	103.63	5	15	40	3.5	184.7	347.8	62.6
916	10H-2, 130	104.41	5	15	40	4.2	184.1	347.2	29.1
917	10H-3, 52	105.13	5	15	40	4.0	188.4	351.5	67.5
918	10H-3, 130	105.91	4	20	40	4.8	94.2	257.3	–1.8
919	10H-4, 52	106.63	5	15	40	3.8	137.0	300.1	–23.8
920	10H-4, 130	107.41	5	15	40	16.0	136.4	299.5	–29.1
921	10H-5, 52	108.13	5	15	40	6.3	189.5	352.6	11.7
922	10H-5, 132	108.93	5	15	40	0.5	220.4	23.5	–3.2
923	10H-6, 52	109.63	5	15	40	7.6	123.5	286.6	33.2
924	10H-7, 46	110.57	5	15	40	4.3	193.5	356.6	63.8
925	11H-1, 52	111.57	5	15	40	2.1	202.1	344.9	–6
926	11H-1, 132	112.37	5	15	40	9.9	305.8	88.6	–29.9
927	11H-2, 52	113.07	5	15	40	9.3	17.2	160.0	–77.1
928	11H-2, 132	113.87	5	15	40	2.4	162.2	305.0	–9.1
929	11H-3, 42	114.47	5	15	40	2.4	275.8	58.6	–19.5
930	11H-3, 90	114.95	5	15	40	7.6	197.4	340.2	28.4
931	11H-3, 142	115.47	5	15	40	1.8	162.8	305.6	–59.9
932	11H-4, 42	115.97	5	15	40	3.2	176.1	318.9	–63.6
933	11H-4, 192	116.47	5	15	40	5.5	131.7	274.5	46.7
934	11H-4, 142	116.97	5	15	40	4.9	151.1	293.9	30.1
935	11H-5, 42	117.47	5	15	40	9.0	115.1	257.9	61.3
936	11H-5, 92	117.97	5	15	40	7.6	36.2	179.0	–35.2
937	11H-5, 135	118.4	5	15	40	2.3	24.5	167.3	45.3
938	11H-6, 42	118.97	5	15	40	9.6	137.1	279.9	–27
939	11H-6, 92	119.47	5	15	40	4.2	144.2	287.0	71.7
940	11H-7, 39	119.94	5	15	40	1.3	247.8	30.6	–7.2
941	12H-1, 43	121.54	5	15	40	2.7	171.1	26.0	69.9
942	12H-1, 92	122.03	5	15	40	2.2	85.4	300.3	66.4
943	12H-1, 142	122.53	5	15	40	3.6	155.5	10.4	76.4
944	12H-2, 42	123.03	5	15	40	2.6	5.9	220.8	50.0
945	12H-2, 92	123.53	5	15	40	8.0	183.2	38.1	70.7
946	12H-2, 142	124.03	4	15	30	5.8	54.6	269.5	69.4
947	15H-4, 102	158.68	4	15	30	9.5	201.3	253.9	–19.4
948	15H-4, 112	158.78	4	15	30	2.1	189.5	242.1	5.3
949	15H-4, 122	158.88	4	15	30	2.3	178.4	231.0	50.8
950	15H-4, 131	158.97	5	15	40	5.2	184.6	237.2	27.1
951	15H-4, 142	159.08	5	15	40	6.3	29.9	82.5	–62.2
952	15H-5, 2	159.18	5	15	40	1.5	183.5	236.1	16.6
953	15H-5, 12	159.28	5	15	40	1.0	159.6	212.2	80.0
954	15H-5, 22	159.38	5	15	40	2.8	106.4	159.0	82.6
955	15H-5, 32	159.48	5	15	40	1.5	51.5	104.1	75.9
956	15H-5, 42	159.58	5	15	40	1.9	43.3	95.9	73.5
959	17H-1, 142	173.81	5	15	40	4.4	209.9	64.0	60.4
960	17H-2, 3	173.92	5	15	40	5.4	158.3	12.4	65.9
962	17H-2, 13	174.02	4	15	40	3.3	214.6	68.7	44.9
	208-1262B-								
963	1HH-1, 127	1.27	5	15	40	11.2	335.7		–31.6
964	1H-3, 52	3.52	5	15	40	1.3	21.8		–26.4
969	2H-1, 52	4.09	5	15	40	2.0	126.0		–40.9
965	1H-3, 127	4.27	5	15	40	2.9	21.2		–35.3
970	2H-1, 127	4.84	5	15	40	3.1	139.5		–41.2

Note: Only a portion of this table appears here. The complete table is available in **ASCII.**

CHAPTER NOTE*

N1. Bowles, J., submitted. Coring-related deformation of Leg 208 sediments from Walvis Ridge: implications for paleomagnetic data. *Phys. Earth Planet. Inter.*

*Dates reflect file corrections or revisions.